



Application of the creeping flow restoration method to an analogue model

Melchior Schuh-Senlis¹, Guillaume Caumon¹, and Paul Cupillard¹

¹RING, GeoRessources / ENSG, Université de Lorraine / CNRS, F-54000 Nancy

Correspondence: Melchior Schuh-Senlis (melchiorschuh@gmail.com)

Abstract.

Structural restoration is commonly used to assess the deformation of geological structures and to reconstruct past basin geometries. For this, most methods use numerical simulations to compute the deformation of geological models from a chosen deformation mechanism for each geological layer, and conditions applied on the boundaries depending on geological knowledge. For example, geomechanical restoration classically uses elastic motion, considers faults as frictionless contact surfaces, and imposes boundary conditions such as interface flattening to estimate the paleo-deformation. To bring more physical behavior and better handle large deformations, we use a reverse time Stokes-based method with negative time step advection. In order to test the method on complex models including various rheology and faults, we apply it to an analogue experiment model. We first show that reasonable restored geometries can be obtained using classical kinematic boundary conditions. We then show that it is possible to relax the imposed kinematic conditions and replace them by more physical boundary conditions. These conditions, however, imply a larger impact of the material properties on the restoration results. Finally, we show that relaxing the boundary conditions and using the previous imposed conditions as choice criteria allows both the assessment of the value of the effective material properties, and the improvement of the restoration results.

15 1 Introduction

The Earth's subsurface is the result of millions of years of deformation. As available data covers at best a few decades, reconstructing the deformation history from the current geometry of a geological region has been a concern for geoscientists. Restoration is an ensemble of methods which aim at this reconstruction by reversing the various processes that have taken place (e.g., Chamberlin, 1910; Dahlstrom, 1969). It covers different procedures and methodologies. The classical techniques in basin analysis are unfolding and unroofing using length/area preservation in order to remove the effects of tectonic forces. In addition to this, several methods have been developed to take into account the effects of other important parameters, like erosion and deposition of sediments (e.g., Dimakis et al., 1998), isostasy compensation (e.g., Allen and Allen, 2013), thermal subsidence due to mantle thermal effect (Royden and Keen, 1980; Allen and Allen, 2013), rock decompaction due to a change



of load (e.g., Athy, 1930; Durand-Riard et al., 2011; Allen and Allen, 2013), or, at a smaller scale, the erosion and deposition
25 of channelized systems (e.g., Parquer et al., 2017). These methods allow us to generate paleo-basin geometries consistent with
present-day observations for use in more elaborate hydro-mechanical forward models (e.g., Bouziat et al., 2019). In this article,
we focus on the structural restoration based on unfolding and unroofing.

Since the beginning of the last century, different methods have been used for unfolding and unroofing models, which can be
classified in three categories. The first category uses geometric and kinematic rules (e.g., Chamberlin, 1910; Dahlstrom, 1969;
30 Gratier, 1988; Rouby, 1994; Groshong, 2006; Lovely et al., 2018; Fossen, 2016). The first implementations in two dimensions
(2D) used balanced restoration (e.g., Chamberlin, 1910; Dahlstrom, 1969; Groshong, 2006). Later on, 2.5D methods such
as map restoration (e.g., Cobbold and Percevault, 1983; Rouby, 1994; Ramón et al., 2016) and finally three dimensional
(3D) geometrical methods were proposed (Massot, 2002; Muron, 2005; Lovely et al., 2018), allowing the tracking of internal
volumetric deformation. These methods, however, considerably simplify rock deformation mechanisms, ignore mechanical
35 layering effects and are extremely limited when considering salt basins. In this light, numerous authors have stressed out
the necessity of incorporating more physical principles into the restoration of geological models (Fletcher and Pollard, 1999;
Ismail-Zadeh et al., 2001; Muron, 2005; Maerten and Maerten, 2006; Moretti, 2008; Guzowski et al., 2009; Al-Fahmi et al.,
2016).

In order to add some mechanical concepts in the restoration process, the second category of methods considers the restoration
40 of sediment layers assumed to deform elastically between frictionless fault surfaces. It has been developed since the 2000s as
a geomechanical simulation with specific boundary conditions (Maerten and Maerten, 2001; De Santi et al., 2002; Muron,
2005; Moretti et al., 2006; Maerten and Maerten, 2006; Guzowski et al., 2009; Durand-Riard et al., 2010, 2013a, b; Tang
et al., 2016; Chauvin et al., 2018). In this approach, internal deformation is not known *a priori*; it is determined from the
mechanical behavior of rocks and the applied boundary conditions. The model is parameterized with elastic properties and the
45 displacement is computed by solving the equation of motion, in which the Cauchy stress tensor is defined by Hooke's law. The
restoration itself is performed by the specific boundary conditions constraining the model. These conditions, usually imposed
on the displacement, rely on assumptions made from the geological knowledge, such as: the uppermost horizon was flat and
horizontal at deposition time and it was not faulted (Chauvin et al., 2018). Although these methods offer significant advances
in the structural restoration of geological models, the boundary conditions set to unfold and unroof the medium are unphysical
50 as the imposed depth of the free surface is the main driver of the deformation (Lovely et al., 2012; Chauvin et al., 2018). As
a result, this restoration approach has overcome some limitations of the geometric restoration process, but it still needs to be
improved to better account for different rheologies, larger deformations, faults, salt tectonics, and boundary conditions.

The last category of methods was introduced in 1999 as a way to improve the restoration of salt structures (Kaus and
Podladchikov, 2001; Ismail-Zadeh et al., 2001, 2004; Ismail-Zadeh and Tackley, 2010). It relies on considering the rocks as
55 viscous fluids to compute the motion, and on applying negative time steps. It is motivated both by the fact that rock salt and
some sediment overburdens behave as viscous fluids over time scales of millions of years, and by the reversibility of the Stokes
equations, which allows the backward time stepping. The first implementations used a linear viscous (Newtonian) rheology
to restore 2D seismic cross-sections of salt diapirs (Ismail-Zadeh et al., 2001), and 3D Rayleigh-Taylor instabilities (Kaus



and Podladchikov, 2001; Ismail-Zadeh et al., 2004). Since then, the method has been used for 3D unfolding in the absence of gravity (e.g., Schmalholz, 2008), extended to non-linear (power-law) viscous behavior (e.g., Lechmann et al., 2010; Fernandez, 2014), or used to study the reverse modelling of flanking structures (e.g., Kocher and Mancktelow, 2005). Schuh-Senlis et al. (2020) have shown the possible extension of the method to sedimentary basins including faults and a non-flat top surface. However, they considered only synthetic models, using the same software, physical laws and material parameters for both the forward and the backward simulations.

65 Considering these methods as a whole, they can be regrouped as numerical simulations which try to restore a model to a previous state in its history. In these simulations, a specific rheology is used to simulate how layers react to surrounding deformation, and specific boundary conditions are used to drive the model deformation. The main issue, in general, is then that the paleo-state of a geological model is not available, so checking the results of the simulations remains problematic.

Analogue modeling tries, with forward experiments, to find the paleo-deformations leading to specific geological structures 70 (Hall, 1815; Ramberg, 1981; Willis, 1894; Cobbold et al., 1989). The idea is to choose materials that present the same deformations as those observed in geological models, but are sufficiently weak to deform at laboratory scales. For example, the experiment presented hereafter in the article has a size around 30 cm × 5 cm and lasts about 3 hours, but the properties of its materials are such that its deformation is similar to that of a sedimentary basin several kilometers wide, over several hundreds of thousands of years. As a result, analog experiments produce structural models where not only the post-deformation state, 75 but also the paleo-state and the deformations the model underwent are known. For this reason, several studies have used them to assess the results of numerical schemes, both forward (e.g., Buiter et al., 2016; Schreurs et al., 2016) and backward (e.g., Chauvin et al., 2018).

In this paper, we investigate the application of the creeping flow restoration to such an analogue laboratory experiment model, including faults and a deformed top surface. The simulations done in this article used the Particle-In-Cell implementation in 80 the FAIStokes code of Schuh-Senlis et al. (2020). Creeping flow restoration is chosen here for three main reasons. First, the deformation is driven by gravity and backward time-stepping, which is assumed more physical. Second, it can handle the rheology of salt layers. Third, it allows the faults to be considered as shear bands with a lower viscosity instead of frictionless surfaces. This allows of change of paradigm from classical restoration schemes trying to impose boundary conditions and rheologies in the restoration simulations. Indeed, the aim of this paper is to show that it is possible to relax the boundary 85 conditions of the simulations, and use the geological knowledge not as conditions but as criteria to check the restoration quality and find the effective material properties in the restored model.

The outline of this paper is as follows: we first present the concepts of Stokes flow-based restoration and the workflow of the FAIStokes code in which we implement it. In a second part, we present the analogue experiment which was used, and the numerical model created from it. In a third part, we start by restoring this model using kinematic boundary conditions, and 90 then introduce new boundary conditions that may add more physical meaning to the restoration. Finally, we use these boundary conditions to assess the impact of the material parameters on the restoration, and we show how to find relevant values for them.



2 Method

2.1 Creeping flow restoration

2.1.1 Stokes flow equations

95 The standard equations for creeping flows are the Stokes equations, consisting of the momentum conservation equation

$$\nabla \cdot \boldsymbol{\sigma} + \mathbf{f} = \mathbf{0} \quad (1)$$

and the mass conservation equation for incompressible fluids (continuity equation)

$$\nabla \cdot \mathbf{v} = 0, \quad (2)$$

100 where ∇ is the del operator, $\boldsymbol{\sigma}$ is the stress tensor, \mathbf{f} is the specific body force (usually the volumetric weight $\rho\mathbf{g}$), and \mathbf{v} is the velocity. The stress consists of a deviatoric part $\boldsymbol{\tau}$ and an isotropic pressure p :

$$\boldsymbol{\sigma} = \boldsymbol{\tau} - p\mathbf{I}, \quad (3)$$

where \mathbf{I} is the identity tensor. In the viscous flow assumption, the deviatoric part of the stress is

$$\boldsymbol{\tau} = 2\eta\mathbf{D}, \quad (4)$$

with η the dynamic viscosity and \mathbf{D} the infinitesimal strain rate tensor defined by

$$105 \quad \mathbf{D} = \frac{1}{2} [\nabla\mathbf{v} + (\nabla\mathbf{v})^T]. \quad (5)$$

Assembling Eq. (1), (3), (4) and (5), the momentum conservation equation can be written

$$\nabla \cdot [\eta(\nabla\mathbf{v} + (\nabla\mathbf{v})^T)] - \nabla p = -\rho\mathbf{g}. \quad (6)$$

110 In sedimentary basins, we usually deal with materials that are highly viscous (with a viscosity η over 10^{17} Pa.s), over time scales of thousands to millions of years, so these equations neglect the inertial part of the Navier-Stokes equations (Massimi et al., 2006). As such, the equations describe a steady-state flow and their resolution provides the velocity of a fluid at a specific position and time. When different fluids are present, the conditions that are applied at their boundaries, as well as their differences in density, can create instabilities such as Rayleigh-Taylor instabilities. These instabilities make the flow non-stationary as they advect the viscosity and density fields in time.

2.1.2 Backward advection

115 In forward simulation schemes, the Stokes equations (6) and (2) are solved for pressure and velocity, and the material representation of the geological model is advected from the velocity at each time step. The simplest way to do it is by using an Euler scheme, the position $\mathbf{x}(t + \Delta t)$ of a given point of the material model after a single time step being computed as

$$\mathbf{x}(t + \Delta t) = \mathbf{x}(t) + \mathbf{v}(t) \cdot \Delta t, \quad (7)$$

where $v(t)$ is the computed velocity of the point at time t (while higher-order methods exist (e.g., Ismail-Zadeh and Tackley, 2010), particularly to stabilize the advection scheme in the case of large time steps, we choose to present the restoration idea with this order one approximation for simplicity). This Finite-Difference approximation relies on the idea that the chosen time step Δt is small enough to approximate the velocity of a particle as a constant over this time step (Δt is usually calculated using a Courant-Friedrichs-Lewy (CFL) condition (Courant et al., 1928)). Since the Stokes equations are linear and do not depend on previous time steps for the computation of the velocity, we can extend this approximation to backward simulations.

This is the basis of backward time stepping restoration schemes: instead of applying Eq.(7), we apply

$$\mathbf{x}(t - \Delta t) = \mathbf{x}(t) - \mathbf{v}(t) \cdot \Delta t \quad (8)$$

for the advection of the points of the material model, at each time step, like in Fig. 1.

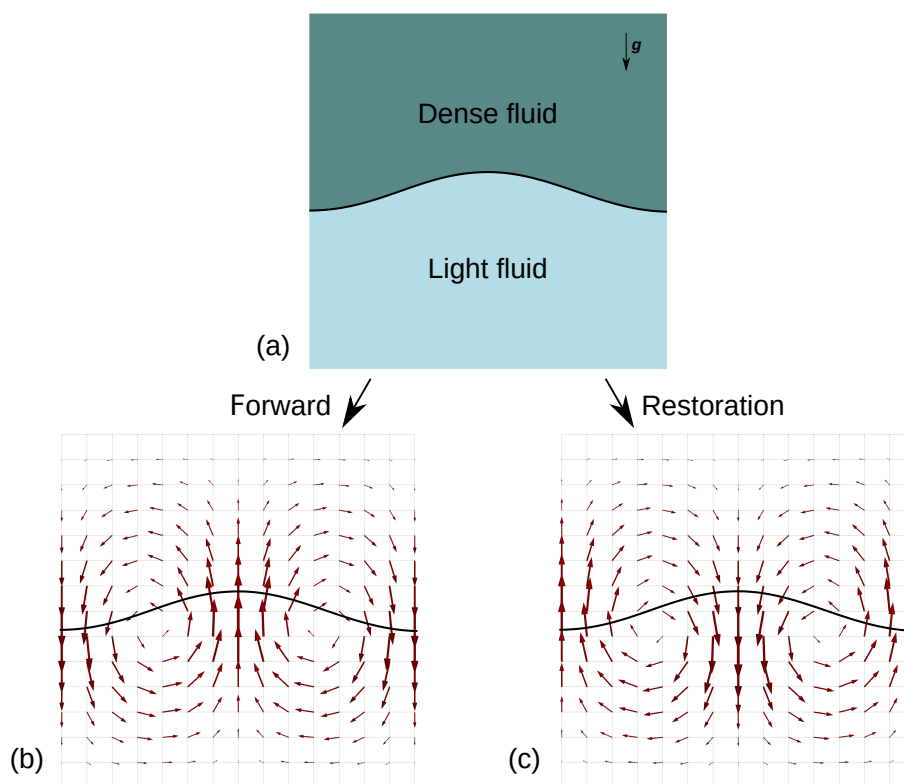


Figure 1. Example of the restoration scheme for a simple setup (a): as the arrows in (b) represent the velocity computed at a specific time step for a forward scheme, the advection of the material model in a restoration scheme is done with the opposite of the computed velocity, shown in (c).

In this light, using viscous fluid properties instead of elastic properties to represent the mechanical behavior of geological materials holds several advantages, such as the use of boundary conditions that are closer to reality, like a free surface on top, or the account of other rheologies like a salt layer.

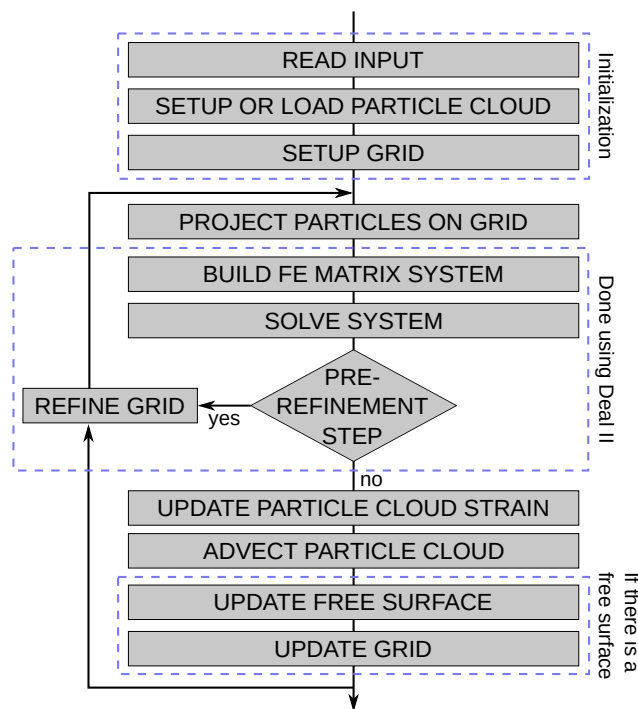


Figure 2. Schematic workflow of the FAIStokes code structure. The pre-refinement step occurs at the beginning of the simulation (or during a reinitialization of the grid) to ensure that the velocity used for the advection step is computed using the adaptively refined grid.

2.2 The FAIStokes code

The restoration scheme presented in the previous section has been implemented in the FAIStokes¹ code described by Schuh-Senlis et al. (2020). It relies on a Particle-In-Cell (PIC) scheme (e.g., Asgari and Moresi, 2012; Thielmann et al., 2014; Gasmöller et al., 2018, 2019; Trim et al., 2020), where the Stokes equations are solved using the Finite Element Method (FEM). The general workflow of the code is shown in Fig. 2, and we here recall its main characteristics.

2.2.1 Material discretization

During mechanical simulations, the material properties inside the model are tracked using particles; each of these particles discretizes the small part of the model around it and its properties. At each time step, the material properties of the particles are interpolated from the particle swarm to the FEM grid in order to build the stiffness matrix and its preconditioner. They are then used to solve the Stokes equations on the grid. Following this, the particles are advected using the solution on the grid.

¹Finite element Arbitrary Eulerian-Lagrangian Implementation of Stokes



2.2.2 Finite Element discretization

In FAIStokes, the Stokes equations are solved on a 2D grid using the FEM algorithms of the deal.II library (Bangerth et al., 2007; Arndt et al., 2019, 2020). Quadrilateral Taylor-Hood $Q_2 \times Q_1$ elements, satisfying the Ladyzhenskaya-Babuška-Brezzi (LBB) condition for stability (Donea et al., 2004), are used. The heat transport equation is not solved.

145 2.2.3 Grid and solvers

The grid and solvers come from the deal.II code. In the right-hand side of Eq. (6), the norm of the gravity vector g of is always 9.81 m.s^{-2} in our simulations, and its direction can be modified to introduce a tilt in the model. The matrix system is solved using an iterative FGMRES solver preconditioned by a block matrix involving the Schur complement (Kronbichler et al., 2012). The grid is adaptively refined and coarsened using deal.II's features, based on the position of the faults and the
150 viscosity variability in the elements. An Arbitrary Lagrangian Eulerian (ALE) scheme is also applied on the grid, as explained in the next paragraphs.

2.2.4 Velocity interpolation

Once the Stokes equations are solved in the domain, the velocity is interpolated on the particle swarm using a Q_2 interpolation scheme. Depending on whether the simulation is forward or backward, the displacement of each particle is computed using
155 either Eq. (7) or (8). The value of the time step Δt is determined from the CFL condition. Finally, the advection is done with a 2^{nd} -order Runge-Kutta scheme in space.

2.2.5 Top surface displacement

The top surface and model interfaces are tracked by separate point swarms in the simulations. These point swarms are denser than the material particle swarm and are one dimension lower (i.e. lines in our 2D cases). They are advected at each time step
160 the same way as the particle swarm that represents the model. After its displacement or during the setup of the grid, the point swarm discretizing the top surface is used as a reference to move vertically the nodes of the grid at the top of the model, so that they match the top surface. This vertical displacement is then propagated to the rest of the grid. The free surface stabilization algorithm proposed by Kaus et al. (2010) is used in all the simulations which consider the top surface as a free surface.

3 Presentation of the analogue model

165 The model we use in this article comes from the deformation of a structural sandbox experiment made by IFPEN² and C&C Reservoirs³, 2016, DAKSTM (Digital Analogs Knowledge System) to reproduce gravity-driven extensional passive margin structures overlaying a salt layer (Fig. 3). Two initial layers were deposited in the model box, forming the pre-growth strata:

²<https://www.ifpennergiesnouvelles.fr>

³<https://www.ccrepositories.com>

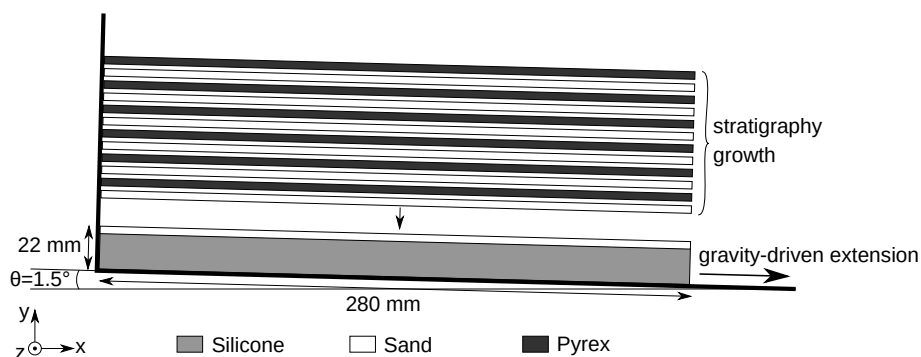


Figure 3. Setup of the creation of the laboratory analogue model. A layer of 18 mm of silicone and a layer of 4 mm of sand are first deposited on a slab with an open boundary. The slab is then tilted with an angle $\theta = 1.5^\circ$, and the layers start to deform with gravity in the direction of the open boundary. During the 256 minutes of the experiment, 12 new layers of alternatively pyrex and sand are deposited, flattening the topography and simulating stratigraphy growth.

a layer of 18 mm of silicone SMG 36 and a layer of 4 mm of sand. The model box was then inclined with a 1.5° angle to simulate a basinward tilt, inducing gravity-driven extension. The experiment lasted for 256 minutes, during which 170 new layers of alternatively pyrex and sand were deposited to simulate stratigraphic growth. These new layers flattened the topography by filling the depressions. The model resulting from the experiment was analyzed using X-ray tomography. This method allows the computation of cross-sections without physically cutting the model. As it is non-destructive, it does not need the consolidation of the model beforehand and avoids the deformation that could occur during the cutting. Moreover, it is dynamic, so it can be used to track the evolution of the experiment. The differentiation of the layers in the cross-sections 175 is done using the difference in density and X-ray attenuation. In our numerical experiments, we made the choice of working at laboratory scale (width of 280 mm and duration of 256 minutes), and we used the known silicone viscosity to reduce the number of parameters to test.

3.1 Available data

Various data are available for this analogue experiment. First, the experiment setup is given, as shown in Fig. 3. Second, the 180 physical properties of the silicone, sand and pyrex layers are known (Table 1). Third, X-ray tomography images are available; they have been taken every two minutes and their resolution is 0.62 mm per pixel. As X-ray tomography is sensitive to density, layer interfaces can be hard to pinpoint where the density contrast is weak. Moreover, no images have been taken during the deposition of sand and pyrex layers, so there are small time gaps at these moments. In the present work, we use a cross-section taken at the end of the experiment (Fig. 4) to test our restoration method. While this implies working in 2D and therefore 185 ignoring out-of-plane displacements, it reduces significantly the computation time for the restoration process, so that more tests on the impact of the different restoration settings can be performed.



Table 1. Physical properties of the silicone, sand and pyrex layers for the analogue experiment. In dark red, the properties that are not relevant due to the difference in rheology between brittle and ductile layers. From the IFPEN documentation on the analogue model experiment (IFP and C&C Reservoirs, 2006).

Physical properties	Sand	Pyrex	Silicone SGM36
Rheological behaviour	Brittle		Ductile (Newtonian)
Density	1.3 - 1.5	1.2	0.97
Grain size (μm)	100-120	80-120	
Internal friction angle	40°	32-36°	
Cohesion (mPa)	0.001-0.002	> 0.005	
Viscosity (Pa.s)			$5 \cdot 10^4$
Natural analogue	brittle rocks (sandstones, limestones)		ductile rocks (salt, undercompacted shales)

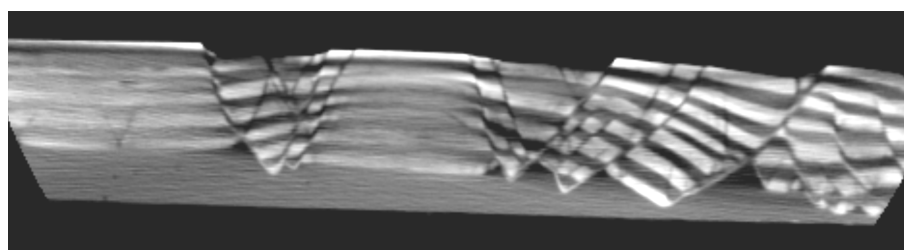


Figure 4. Final cross-section of the analogue experiment. The image has been obtained using X-ray tomography, with a resolution of 0.62 mm per pixel. As the range of the imaging is limited, the borders of the experiment are not present on the image.

3.2 Creation of the numerical model

To digitize the cross section in Fig. 4, we first rotate it left by 1.5° to horizontalize the model base and cut to a rectangular shape. A graphical user interface developed for FAIStokes is then used to digitize the interfaces and the faults in the cross-section. Finally, a particle swarm is created, and the fault and interface lines are used to define the layers and determine the material properties of the particles. The particle swarm contains 667087 particles at the beginning of the restoration, with a distance of 0.14 mm between each particle.

In the faults, the viscosity of the particles is minimal at the position of the fault line (representing the fault core), and increases with a power-law until reaching the fault border. The distance between the fault core and the fault zone border, defining the shear band thickness, is different for each fault (Table 2). Indeed, a close look to the cross-section in Fig. 4 shows that each fault has a different range of deformation around its core.

The obtained numerical model can be seen in Fig. 5. To restore it, the times between each layer deposition in the forward (laboratory) experiment are used as the restoration durations (Table 3) after which the particles at the top are stripped off. The



Table 2. Shear band thicknesses of the fault in the analogue model. The values come from the analysis of the final cross-section (Fig. 4). The index of each fault is given in Fig. 5. The faults with two values have a shear thickness that is reduced at the top of the model because they have a lower deformation range there.

Fault index	Shear band thickness (mm)
1	2.2
2	1.4
3	1.8
4	2.1
5	1.2-2
6	1.2-1.8
7	1.6-3
8	1
9	1
10	1
11	1
12	1.6
13	1
14	1.4
15	1

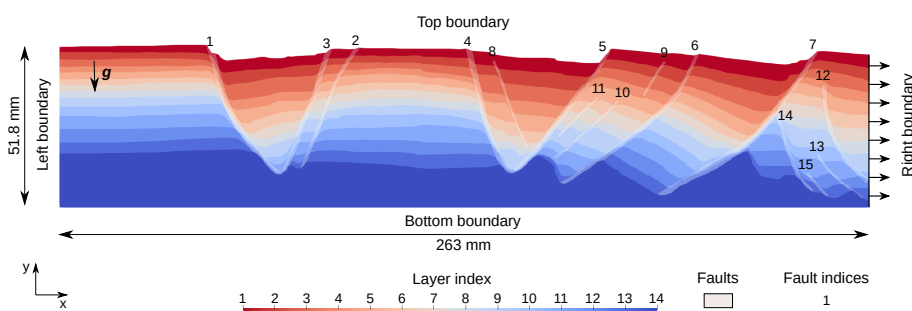


Figure 5. Setup of the analogue model to input in FAISStokes for the restoration simulations. The model boundary conditions are not specified here, as their choice and impact on the simulations are discussed in the next section. During the simulations, the tilt of the model is introduced by rotating the gravity vector, as explained in Section 2.2.3.

X-ray tomography images are also used to determine the height of the topography after the deposition of each layer. This height is used, in some cases, to impose a flattening condition on the top surface of the model.



Table 3. Duration of the restoration simulation and topography height after deposition of each layer of the analogue model. The indices of the layers are shown in Fig. 5.

Layer index	Simulation duration (minutes)	Topography height (mm)	Material
1	18	52.6	sand
2	12	50.06	pyrex
3	16	48.26	sand
4	16	45.71	pyrex
5	16	44.68	sand
6	14	42.38	pyrex
7	14	40.09	sand
8	12	38.55	pyrex
9	10	37.27	sand
10	18	33.7	pyrex
11	14	31.14	sand
12	16	26.8	pyrex
13	14	22	sand
14	(pre-growth layers)	18	silicone

Table 4. Material properties of the silicone, sand and pyrex layers in the restoration simulations which assess the impact of different boundary conditions. In red, the density of the particles inside the faults is the same as the density of the layer to which they belong. The grey cells show the values that come from the laboratory experiment.

Material properties	Sand	Pyrex	Silicone SGM36	Fault core
Density	1.4	1.2	0.97	
Viscosity (Pa.s)	$5 \cdot 10^5$	$5 \cdot 10^5$	$5 \cdot 10^4$	$5 \cdot 10^4$

4 Boundary condition analysis

In geomechanical restoration, specific boundary conditions have been used, such as flattening the top surface or tying the fault lines to remove fault throw (Muron, 2005; Chauvin, 2017). Because viscous behavior cannot be handled by elastic motion, the interfaces with basal salt layers have usually been considered as free surfaces (e.g. Stockmeyer and Guzowski, 2014). Here, we start with simple boundary conditions and show their impact on the motion inside the model and how they can be upgraded to more physical assumptions. The material properties of the layers are not studied here (they will be covered in Section 5), so we consider them as constant in the simulations presented in this section (Table 4). The density of the layers comes from the data (Table 1), and the density of the particles inside the faults is assumed to be the same as in the rest of the layer they belong to. The viscosity of the silicone is known, and we set the viscosity of the sand and pyrex as ten times higher. The viscosity at the fault core is set to be the same as inside the silicone.



4.1 Restoration using kinematic boundary conditions

The first boundary conditions we test are kinematic. The bottom and left boundaries are set to free slip. For each layer, the top surface is flattened using a Dirichlet condition: the vertical component of the velocity on the top nodes of the grid at time t is set to

$$215 \quad v_y(n, t) = -\frac{Y_{final} - y(n, t)}{T_{simulation} - t}, \quad (9)$$

with n the index of the node, $y(n, t)$ its altitude, $T_{simulation}$ the duration of the restoration for the current top layer, and Y_{final} the height of the topography at the end of the restoration of the layer (determined from the tomography images and shown in Table 3). The velocity 9 is in the opposite direction of the final altitude, as it is then applied with a backward advection scheme. The right boundary is set to a fixed flow. As we consider incompressible flow, the kinematic conditions must ensure
220 the conservation of model volume during the simulation. This means that the volume change due to the topography evolution ΔV_{top} must be compensated by the volume entering at the right boundary ΔV_{right} :

$$\Delta V_{top} = \Delta V_{right}. \quad (10)$$

Using the CFL condition, the time step should be computed from the velocity field at each time iteration. This is an issue here, because ΔV_{top} depends on the time step (computed from the velocity field), and the horizontal velocity at the right boundary
225 determined from ΔV_{right} is necessary for the computation of the velocity field. To get rid of this dependency, we impose a fixed time step Δt such that the volume change is constant:

$$\Delta V_{top} \simeq \frac{V_f - V_i}{T_{simulation}} \Delta t = \text{constant}. \quad (11)$$

The horizontal flow at the right boundary was then applied as

$$v_x(t) = \frac{\Delta V_{right}}{Y(t)\Delta t} = \frac{V_f - V_i}{Y(t)T_{simulation}}, \quad (12)$$

230 with $Y(t)$ the altitude of the upper right corner of the model.

The result at the end of the restoration of each layer is shown in Fig. 6. As imposed by the boundary conditions, the topography at the end of each layer restoration is flat, and the fault throw is reduced for all the faults. The restoration behaves well for the first layers, but has more difficulty restoring the oldest layers, which accumulated more deformation: even though the sand and pyrex layers are expected to become increasingly flat during the restoration, they accumulate more folding.
235 Likewise, the silicone diapirs tend to go upwards whereas they are expected to go downwards to flatten the sand/silicone interface. This is due to the model accumulating computation errors, as well as errors coming from the simplifications we made (on the interfaces during the digitization of the model, on the material flowing from the right boundary and on the material properties inside the different layers for example). Another issue with the use of complete kinematic conditions is the resulting over-parameterization of the system, making it prone to over-steps in the velocity if the volume flow is not perfectly
240 balanced. The fixed time step can, for example, result in particles moving out of the model boundary in the advection step because the CFL condition is not met.

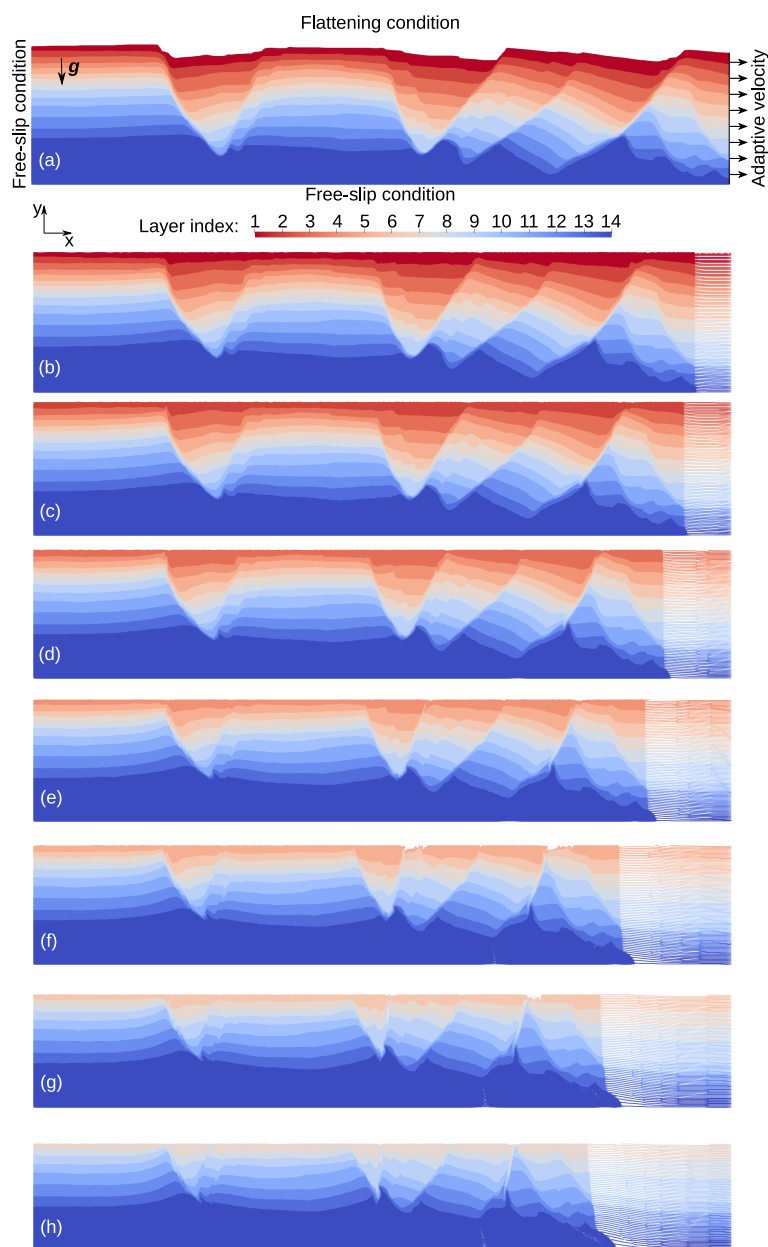


Figure 6. Results of the restoration of the successive layers of the analogue model. In this case, the bottom and left boundaries have a free-slip condition, the top is flattened to the topography height at layer deposition, and the right boundary has a velocity condition which adapts to the flattening condition, based on Eq. (12). (a) shows the setup at the beginning, and (b) to (h) show the state of the model at the end of the restoration of each layer.

To assess the restoration of the layers below the surface, the tomography image taken after the deposition of the last layer is compared to the position of the restored interfaces at this time (Fig. 7). The tomography image is digitized, allowing the

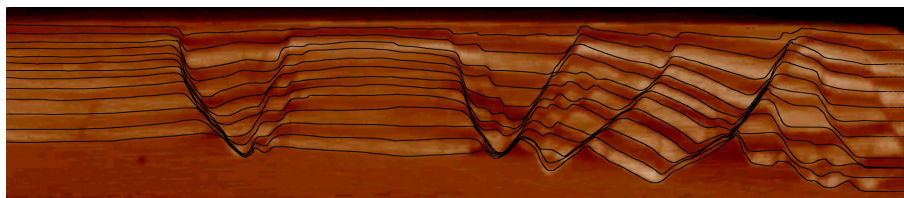


Figure 7. Comparison between the cross-section image taken by X-ray tomography after the deposition of the last layer (shown in background), and the restored interfaces at that time (shown as superimposed black lines). The restoration here is performed using the kinematic conditions defined in section 4.1.

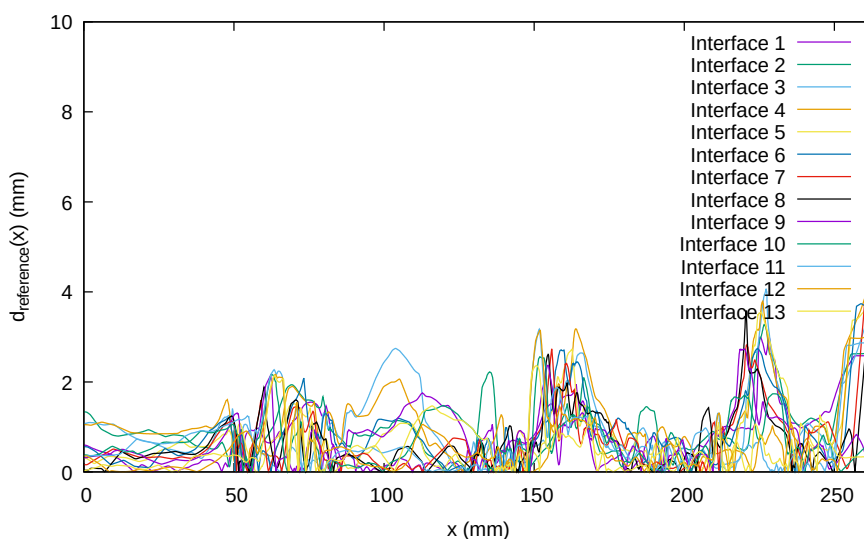


Figure 8. Distance, for each interface between two layers of the model, between the restored interface at the end of the restoration of the first layer, and its actual state at this time, digitized from the corresponding cross-section. The restoration here is performed using the kinematic conditions defined in section 4.1. The interface index corresponds to the index of the layer directly above (see Fig. 5). The digitization of the cross-section has an accuracy of around 1 mm.

245 computation of the vertical distance $d_{reference}(x)$ between the restored interface and the actual state of the interface (serving as the reference) at that time, with x the position along the horizontal axis. This distance gives a measure of the error in the restoration of each interface. It is shown in Fig. 8, along with the integral of this distance on the horizontal axis.

Using these results, we see that the error is overall less than 4 mm, which is acceptable considering the size of the model (52×263 mm) and the accuracy of the cross-section digitization (around 1 mm). The largest errors appear at the right boundary, where the new material entering during the restoration is not known, introducing a high uncertainty on the resulting interfaces.



Table 5. Integral, for each interface between two layers of the model, of the distance between the restored interface at the end of the restoration of the first layer, and its actual state at this time, digitized from the corresponding cross-section. The restoration here is done using the kinematic conditions defined in section 4.1. The interface index corresponds to the index of the overlying layer (see Fig. 5).

Interface	1	2	3	4	5	6	7	8	9	10	11	12	13
$\int d$ (mm ²)	191	251	258	289	207	223	178	174	188	177	181	157	130

250 Overall, these first results are encouraging, as they show the potential of the creeping flow restoration method when applying it to sedimentary basin analogues. One downfall, however, is that the boundary conditions are not natural, which raises doubts about the physical realism of the resulting strain.

4.2 Upgrading the kinematic conditions to natural boundaries

255 This section aims at improving the unphysical right and top boundary conditions. Indeed, in the previous subsection, the right boundary was considered as having a constant flow, where the flow should in principle depend on the altitude. Moreover, the top surface was set to flattening although it corresponds to a free surface.

4.2.1 Relaxing the right boundary condition

In order to remove the over-parameterization of the model and add more natural boundary conditions, one can change the right boundary condition to a Neumann traction condition instead of a Dirichlet velocity condition. The weight of the materials on the right side of the model can then be accounted for by introducing a traction based on the pressure on the right boundary. Here, the traction we use is based on the lithostatic pressure $p(x, y)$ inside the model:

$$p(x, y) = p_0 + \int_y^{y_{max}(x)} \rho(x, y) \|\mathbf{g}\| y dy, \quad (13)$$

with p_0 the pressure at the surface of the model (neglected here after). In the case of our analogue model, we consider a constant gravity vector \mathbf{g} and the density as constant in each layer, which makes the lithostatic pressure piecewise linear (Fig. 9). The Neumann traction condition applied on the right boundary is then defined as:

$$\mathbf{h}_N(y) = -\nu p(x_{max}, y) \mathbf{n} \quad (14)$$

where the Poisson coefficient is taken as $\nu_{overburden} = 0.4$ in the sand and pyrex layers and $\nu_{silicone} = 0.5$ in the incompressible silicone layer, and \mathbf{n} is the outward unit normal vector of the right border.

270 The results for the successive restoration of the layers with this traction are not shown, as they are similar to those in Fig. 6. However, we show in Fig. 10 the distance between the restored interface at the end of the restoration of the first layer and the actual state of the interfaces at that time, along the horizontal axis. The integral of this distance along the horizontal axis is also computed.

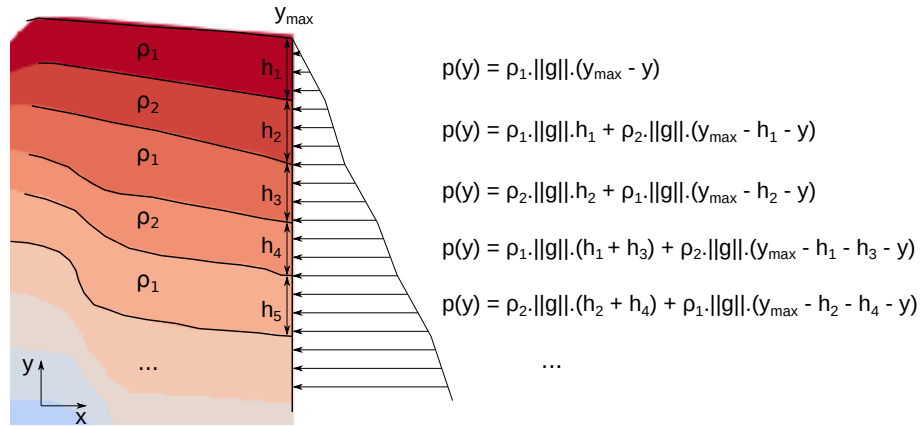


Figure 9. Computation of the lithostatic pressure at the right boundary of the analogue model. A $\cos(\theta)$ factor is then added to the value to take into account the impact of the model tilt on the boundary.

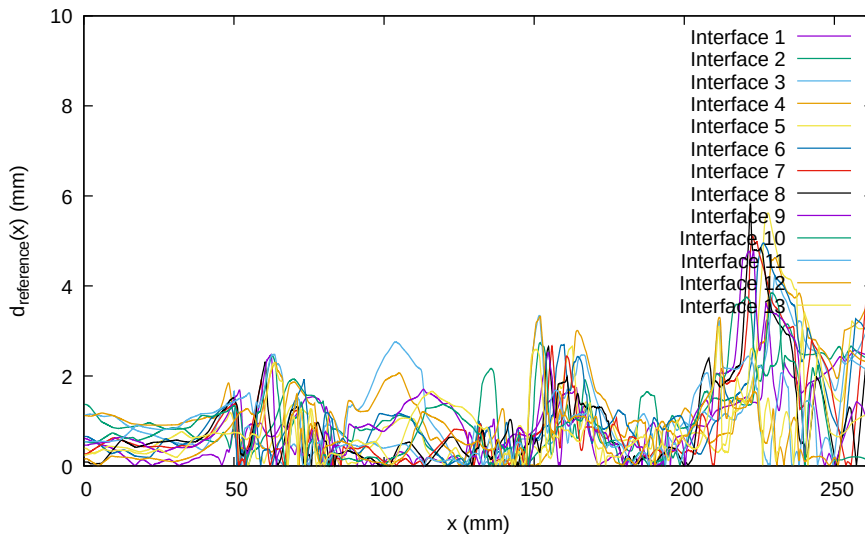


Figure 10. Same as Fig. 8 with the Neumann condition defined in Eq. (14) on the right boundary.

While imputing this new condition on the right boundary gives it more physical sense, it also increases the freedom of the model and its sensitivity to the material properties. The slight increase of the error in the restoration of the interfaces, as compared to the fully kinematic boundary conditions, could then come from inaccurate material properties inside the model. This hypothesis is also supported by the following results.

275



Table 6. Integral, for each interface between two layers of the model, between the restored interface at the end of the restoration of the first layer, and its actual state at this time, digitized from the corresponding cross-section. The restoration here is done using the Neumann condition defined in Eq. (14) on the right boundary. The interface index corresponds to the index of the layer directly above, from the indexation of Fig. 5.

Interface	1	2	3	4	5	6	7	8	9	10	11	12	13
$\int d$ (mm ²)	211	293	313	346	264	289	245	242	264	247	240	193	207

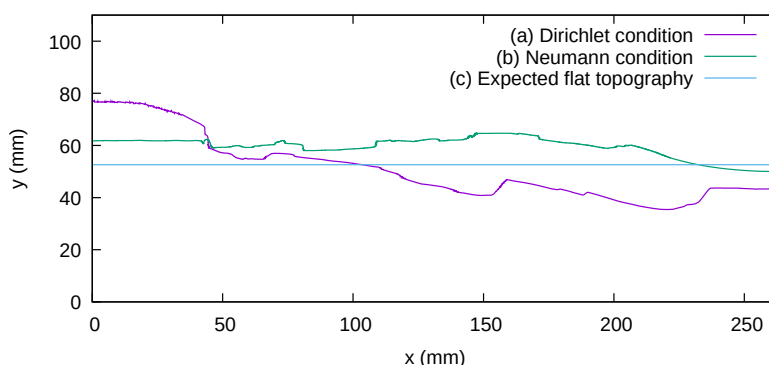


Figure 11. Impact of the boundary conditions on the top surface topography, after a few hundred time steps of restoration. The bottom and left boundaries have a free-slip condition and the top is a free surface. The right boundary condition is either (a) a constant flow based on Eq. (12) or (b) the Neumann condition defined in Eq. (14). The expected flat topography is given in (c) as a reference. We see that unphysical Dirichlet condition deforms the topography by bringing up the left part of the model and bringing down the right part of the model. On the contrary, using the traction based on the lithostatic pressure, the whole model is brought up and the fault throws are reduced. We can see, however, that the material properties inside the model do not restore it properly: the top surface ends up higher than expected.

4.2.2 Relaxing the top surface condition

In the previous simulations, the goal was to test if the model could be restored with creeping flow simulations and a classical topography flattening boundary condition, and to estimate the impact of the lateral boundary condition. While it makes the top surface go back to the state it was at deposition time, it is unphysical (Lovely et al., 2012). Indeed, as the topography of the model is in contact with air during the analogue experiment, a free surface condition should be set on it. Moreover, flattening means imposing a Dirichlet condition, but the velocity of the topography through time is not known, so an assumption has to be made (we here assume a constant velocity). Enforcing a velocity condition also makes it unsure whether the other model parameters are relevant or if they just scale well with the imposed deformation. For example, Fig. 11 shows the top surface of the model after some time steps, when it is treated as a free surface (i.e., only gravity and the right boundary drive the deformation). We can see that imposing the traction 14 on the right boundary condition is necessary to balance the model properly, or the topography becomes steeper instead of becoming flat during the deformation. When the condition on the right

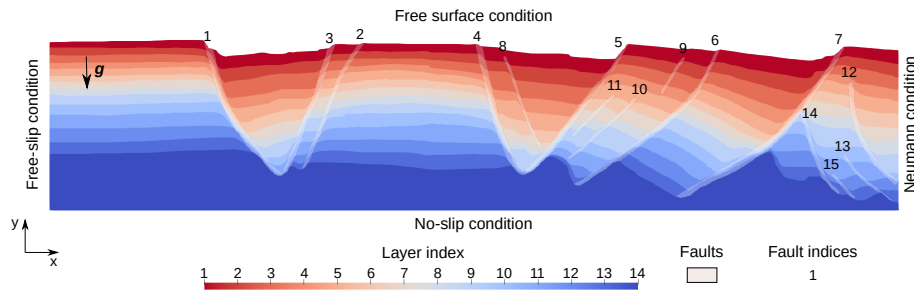


Figure 12. Setup of the analogue model to assess the impact of the material properties on the restoration simulations. The right boundary uses the Neumann condition defined in Eq. (14).

boundary is set to a traction based on the lithostatic pressure, the fault throws of all the faults are reduced during the simulation, and the topography comes closer to being flat. While this is encouraging, the model is still not restored properly, as the model deformation is not consistent with the analogue experiment, where the velocity is lower. This is due to the material properties inside the model being incorrect, and particularly the sand and pyrex viscosities being too low.

5 Model parameters analysis

5.1 Rough estimation of the material properties

In the previous section, the impact of the boundary conditions on the restoration of the analogue model was discussed. It suggested that finding relevant effective material properties was necessary to improve the restoration process. In this section, the material properties that come from the data (shown in the grey cells of Table 4) are considered as known and we look for the effective viscosity of the sand and pyrex layers. The boundary conditions are set as shown in Fig. 12. The left boundary is set to a free-slip condition; the bottom boundary is set to a no-slip condition; the right boundary uses the Neumann traction condition defined in Eq. (14); the top boundary condition is set to a free surface. Doing so, the impact of the choice of material properties on the simulation can be assessed without enforcing the velocity on any boundary.

As most of the material properties are given as data, only the viscosity of the sand and pyrex layers are left as unknowns. For simplicity, the viscosity is considered as homogeneous in each layer (outside the faults), with the same value in all the layers no matter whether they are in sand or pyrex. In the faults, the applied viscosity is minimal at the core and increases with a power law up to the contact with the rest of the layers. The range of the viscosity of the sand and pyrex (hereafter called “overburden viscosity”) is chosen as $[10^5 : 10^7]$ Pa.s, in order to have a viscosity ratio between the silicone and the overburden in the range of $[2 : 2.10^2]$. The range of the fault viscosity is chosen as $[5.10^3 : \eta_{overburden}/2]$ Pa.s. Eight experiments are conducted, following the parameter choice shown in Fig. 13 for the viscosity of the overburden and faults.

To check the quality of the restoration for each experiment, various criteria can be applied. Here, the implemented criterion corresponds to the area between the topography of the model at any point x in the restoration and the expected topography after

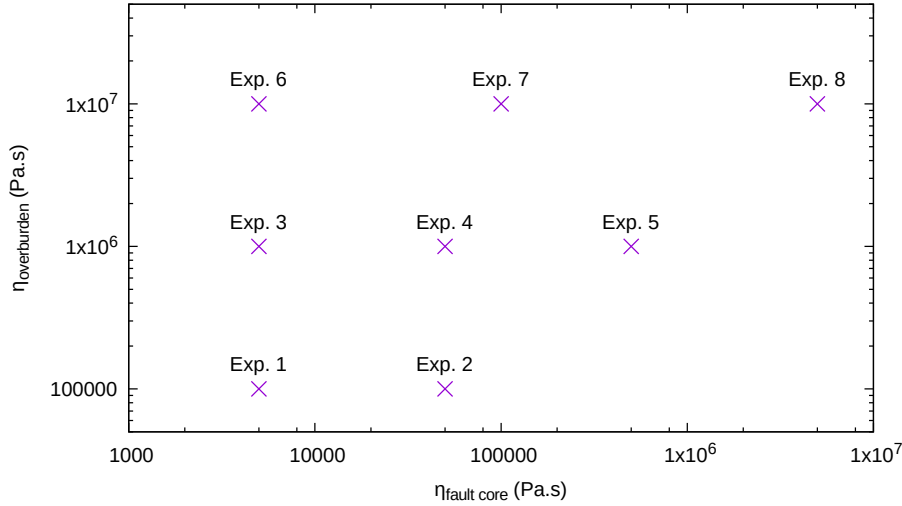


Figure 13. Design of experiments to estimate the effective material properties of the analogue model.

310 the restoration of the first layer. It allows a tracking and comparison of the results throughout the simulation. It is computed as:

$$C_{expected\ horizontality}(t) = \int_0^{x_{max}} |y_{top}(x,t) - y_{expected}| dx, \quad (15)$$

where x_{max} is the domain length, $y_{top}(x,t)$ is the altitude of the topography along the x axis at a given time t , and $y_{expected}$ is the expected altitude of the topography at the end of the restoration of the layer (from Table 3). This criterion is hereafter referred to as the expected horizontality criterion. It has several advantages: first, it is relatively simple to compute and track throughout the restoration simulations. Second, it gives a value of the global difference between the model and the expected restoration result with a flattened top layer. Third, it can be used to compare simulations which evolve at different velocities, and to check when they start to evolve in the wrong direction (i.e., creating relief in reverse time).

The values of the expected horizontality criterion through time for the eight experiments are given in Fig. 14. In all the experiments, we can see that the model deformation starts by going towards a flat topography at the expected altitude (the expected horizontality criterion decreases towards zero). In experiments 1 to 3, after some time this behavior changes and the model topography evolves away from the expected altitude. In the other experiments, the expected horizontality criterion decreases, but does not reach zero before the end of the layer restoration. In experiments 1 to 3, we let the simulations continue after the criterion started to increase, for testing purposes. Such an increase could, in practice, be used to detect when a restoration simulation is wrong (because of computational instabilities like those shown in Section 4.2.2 for example) and to stop the simulation.

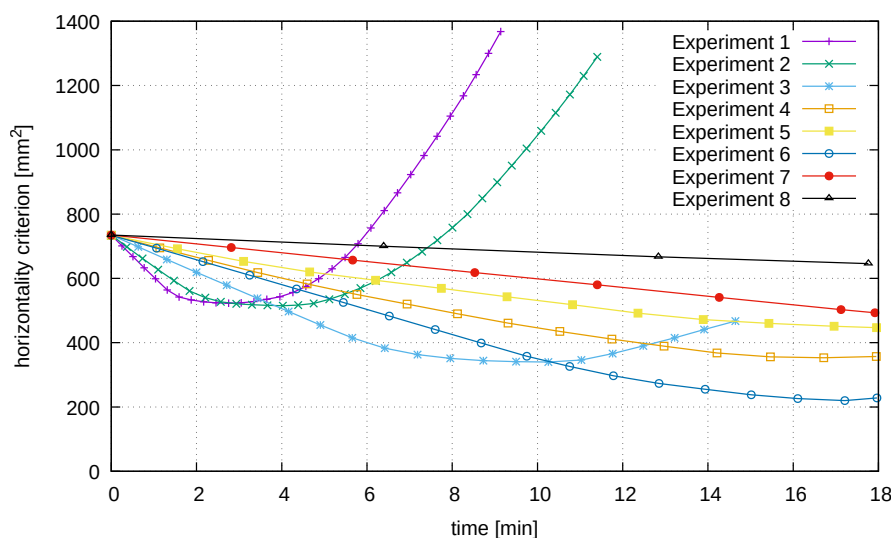


Figure 14. Values of the expected horizontality criterion (Eq. (15)) throughout time for the simulations of the design of experiments (Fig. 13) to find the effective material properties inside the analogue model.

While the expected horizontality criterion is good to determine the global distance between the simulations and the expected result, it is not enough to determine the ‘best’ material parameters for the restoration. Figures 15 and 16 show the state of the model for each experiment at the time t_{final} of their last point in Fig. 14, in order to analyze the impact of each parameter
330 involved in the design of experiments in a more detailed way.

In experiments 1 and 2, the rapid increase of the expected horizontality criterion is explained by the right part of the model going up. The overall restoration also shows that the thicknesses of the overburden layers increase too much, while the fault throws are not reduced much during the simulation. It can be explained by the viscosity of the overburden being too low as compared to the viscosity of the faults. In experiment 3, we observe that the fault throws are overall reduced, but some of them
335 get inverted (on faults 2, 6 and 7, with the numbering of Fig. 5), suggesting that the viscosity of these faults is too low. In experiment 4, as in experiments 1 and 2 (but not in the same proportions), the deformation of the left and right parts of the model is a bit strong, while the fault throws are not reduced much, showing that the viscosity of the faults is not low enough, while the viscosity of the overburden is too low. In experiment 6, the fault throws are overall reduced or canceled. Although it shows the smallest value of the expected horizontality criterion (Fig. 14), faults 2, 6 and 7 (with the numbering of Fig. 5) start
340 to invert their throw, like in experiment 3, showing that their viscosity is too low as compared to the viscosity of the overburden. In experiments 7 and 8, the overall deformation is too small, showing that the viscosity of both the overburden and faults is too high.

The results of these experiments show that it is possible to narrow down the possible values of the effective parameters in this type of model. It also shows, however, that the viscosity of the materials at play cannot be modeled by a unique value for

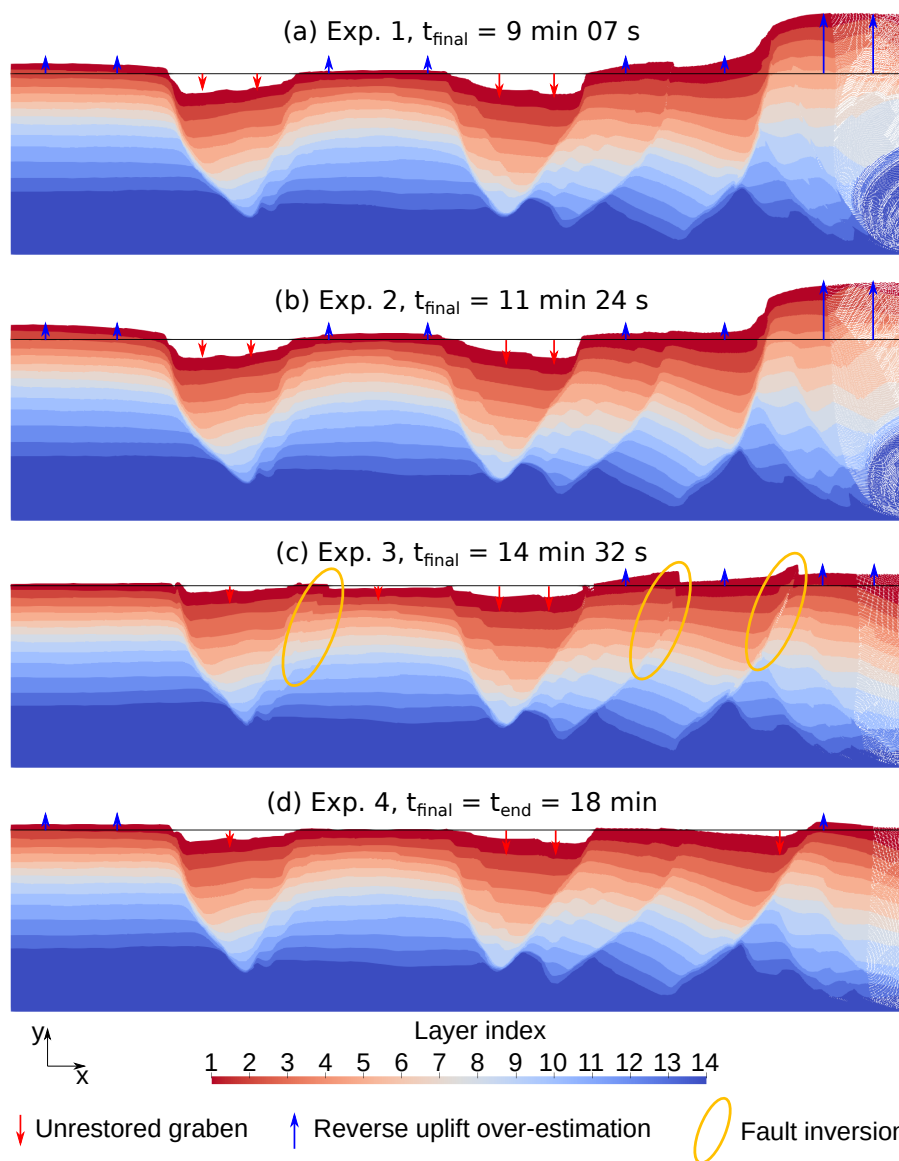


Figure 15. Results of experiments 1 to 4 (Fig. 13) to find the effective material properties inside the analogue model. For each experiment, t_{final} is the restoration time at which the simulation is stopped, and for which the model is shown. t_{end} is the time at the end of the restoration of the first layer. The black line on each result is the expected position of the topography at the end of the restoration of the first layer.

345 all the material types. Particularly, the viscosity should differ from one fault to the other: as their histories differ, so do their mechanical properties.

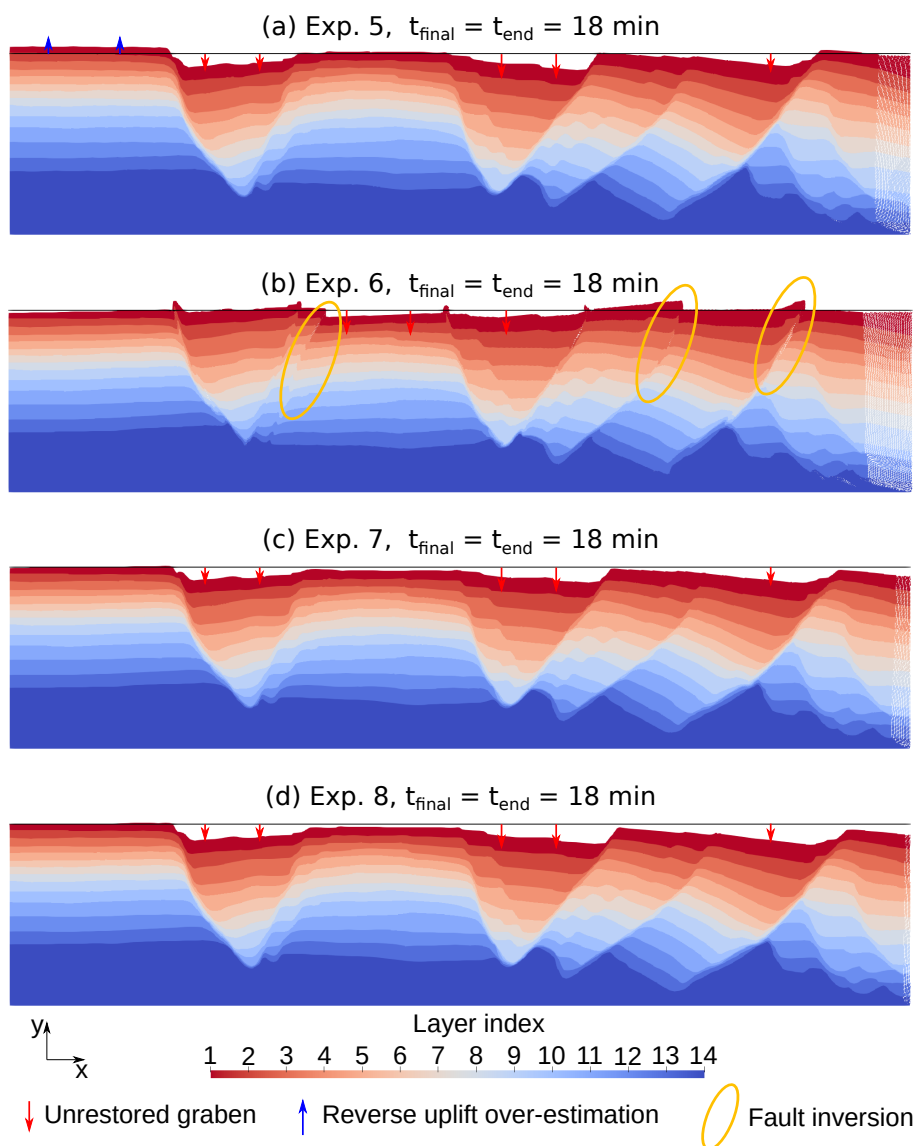


Figure 16. Same as Fig. 15 for experiments 5 to 8.

5.2 Fine tuning of the material parameters

Given the previous results, the viscosity of the faults looks like an important parameter to improve restoration. More specifically, the fault inversion appearing only on some faults in experiments 3 and 6 calls for a specific treatment of each fault. In the following, we carry out tests to estimate the viscosity within each fault. The material properties that were considered as known in the previous section do not change (see the grey cells of Table 4). Based on the previous results, the viscosity in the overburden layers is set to $8 \cdot 10^6$ Pa.s, and the default viscosity at the core of the faults is set to $5 \cdot 10^3$ Pa.s. Starting from this

350



Table 7. Factors to multiply the default fault core viscosity to obtain the best restoration result. The fault indices are defined in Fig. 5.

Fault index	1	2	3	4	6	7
Multiplying factor	0.75	7	3	2	7	3

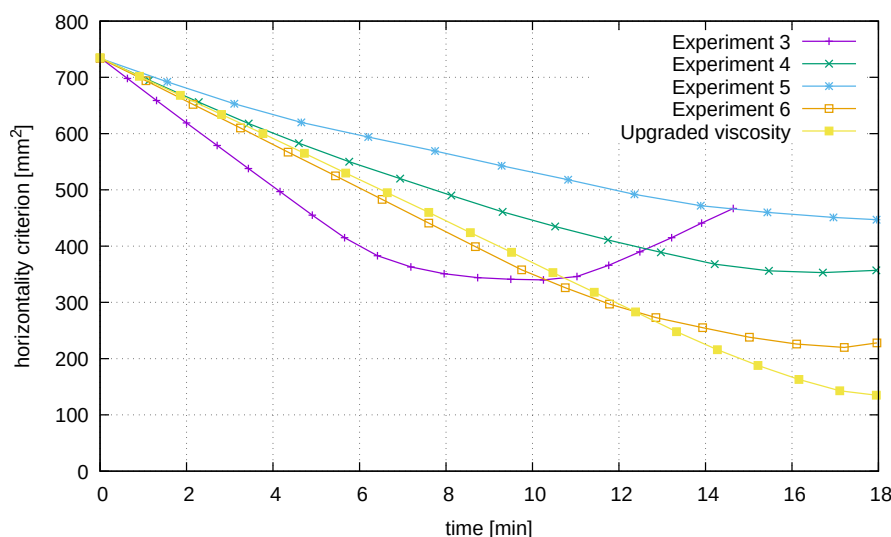


Figure 17. Values of the expected horizontality criterion (Eq. (15)) through time for the restoration with a fine tuning of the fault viscosity (yellow curve), as compared to some experiments of Section 5.1.

default value, various tests are performed by multiplying it by different factors (from 0.75 to 3) in each fault. The factors which give the best restoration results are shown in Table 7. For this restoration, the values of the expected horizontality criterion as a function of time are compared to previous results (Fig. 17). They show that a finer analysis of each fault upgrades the global restoration and makes the model closer to being flat at the end of the restoration simulation. In order to look at a more global criterion, Fig. 18 shows the comparison between the tomography image taken after the deposition of the last layer and the position of the restored interfaces at this time. Additionally, Fig. 19 shows, for each layer interface, the vertical distance between the restored interface and the actual state of the interface at that time, along the horizontal axis. The integral of this distance along the horizontal axis is given in Table 8. Overall, the analysis of the restored interfaces yields lower restoration errors than with fully kinematic boundaries. Both the visual (Fig. 18) and quantitative comparisons of the X-ray tomography image and the restored interfaces show that the restoration is better on most of the interfaces. The highest errors come from the faults, where the low viscosity induces a “squeezing” effect on the material inside the shear band during the simulation, resulting in an upward motion at their position, particularly near the top of the model.

These results show that it is possible to obtain better restoration results than those obtained with kinematic conditions, while also being more physical and giving valuable information on the effective viscosity to apply in numerical simulations of viscous-based models.

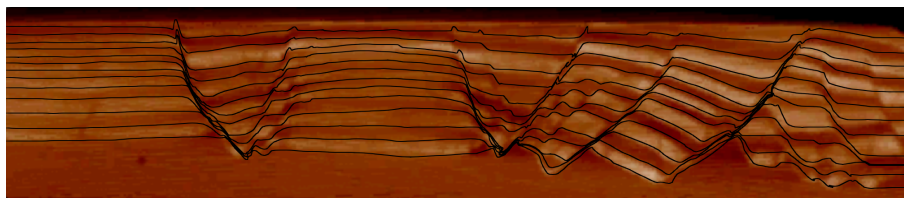


Figure 18. Comparison between the cross-section image taken by X-ray tomography after the deposition of the last layer (shown in background), and the restored interfaces at that time in the restoration process (shown as superimposed black lines). The restoration here is done using the boundary conditions and model parameters of section 5.2.

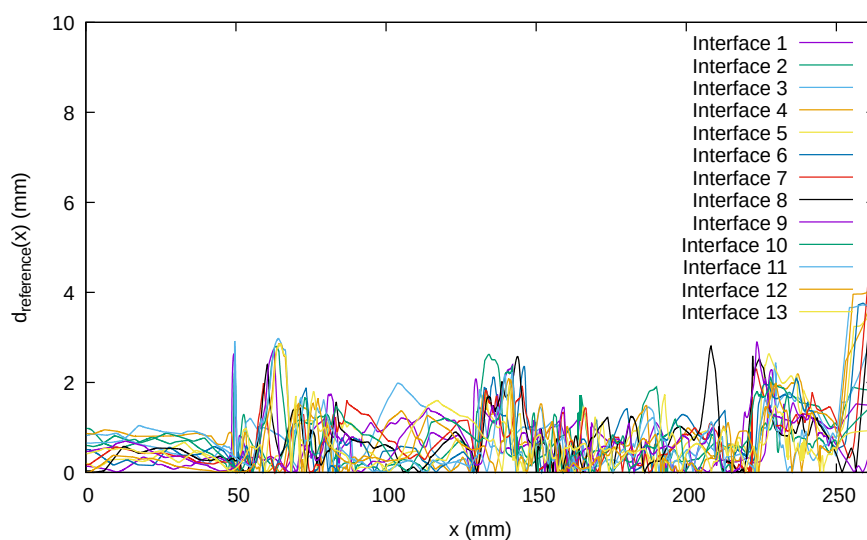


Figure 19. Same as Fig. 8 with the boundary conditions and model parameters of section 5.2.

6 Discussion

Previous restoration approaches have shown that geomechanical schemes can be used to add physical meaning to the restoration process (e.g., Maerten and Maerten, 2001; Muron, 2005; Moretti et al., 2006; Durand-Riard et al., 2010; Chauvin et al., 2018), and account for specific rheological behavior such as that of salt rock (e.g., Kaus and Podladchikov, 2001; Ismail-Zadeh et al., 2001, 2004). Recently, Schuh-Senlis et al. (2020) showed that creeping flow restoration could be applied to synthetic basin models which include salt, faults and a free surface condition at the top. To go further, we here applied the restoration process of Schuh-Senlis et al. (2020) to an analogue experiment model. This allowed us to test the results of the creeping flow restoration method on a model obtained by the deformation of an actual material. The deformation history images on a cross-section were used to quantify the accuracy of the restoration results, and some reference rheological values of the laboratory analogue experiment (e.g., salt viscosity) were introduced in the numerical model to make our test simpler.



Table 8. Integral, for each interface between two layers of the model, between the restored interface at the end of the restoration of the first layer, and its actual state at this time, digitized from the corresponding cross-section. The restoration here is done using the Neumann condition defined in Eq. (14) on the right boundary. The values of the same distance computed for the restorations of sections 4.1 and 4.2.1 are reminded, for comparison. The interface index corresponds to the index of the layer directly above, from the indexation of Fig. 5.

Interface index	1	2	3	4	5	6	7	8	9	10	11	12	13	Total
$\int d$ (mm ²) (Free boundaries & effective parameters)	170	190	203	225	189	198	200	196	178	204	200	174	165	2492
$\int d$ (mm ²) (Kinematic restoration)	191	251	258	289	207	223	178	174	188	177	181	157	130	2604
$\int d$ (mm ²) (Flattening & Neumann)	211	293	313	346	264	289	245	242	264	247	240	193	207	3354

In the analogue model on which the restoration method is applied, the viscosity is as low as $5 \cdot 10^3$ Pa.s and time-scales range from seconds to hours. While neglecting the inertial part of the Navier-Stokes equations at these scales is questionable, this hypothesis is supported by three points. First, the displacement during the experiment is sufficiently slow to neglect any inertial effects. Second, the restoration results back up this assertion. Third, this is a limit-case to test the validity of the method on an analogue experiment, and the application on the corresponding geological model would verify the hypothesis, as stated in Sect. 2.1.1.

The first tests on the analogue experiment model showed that the first layers of the model could be restored properly with kinematic boundary conditions such as those used in standard geomechanical restoration. More natural boundary conditions were then tested, namely a Neumann traction condition on the right boundary, which accounts for the lithostatic pressure, and a free surface condition on the top surface of the model. Some erratic results obtained with these more realistic boundary conditions suggest that they can be used to detect errors in some model parameters (e.g., other boundary conditions or material properties).

The case of the left and bottom boundaries has not been discussed much. The first tests (Section 4) used a free-slip condition on both surfaces, and the simulations in the design of experiments (Section 5) changed the bottom boundary to a no-slip condition. These assumptions are simplifications, and a friction condition on the bottom and a Neumann condition on the left-hand side might be more physical. Several tests showed, however, that the difference between a free-slip and no-slip condition on the two boundaries impacted the simulations only if they were otherwise unbalanced (by a wrong traction on the right boundary, for example).

For the right boundary traction, the Poisson coefficient was set from reference values for the type of granular material in the model, but it may have to be estimated more properly and more precisely. Indeed, additional tests have shown that while the Poisson coefficient value does not impact the general behavior of the model, it can impact the value of the ‘best’ effective viscosity inside the model. Another possible issue with the traction at the right boundary of the model is the account of the tilt and its implications on the material on the other side of the boundary. Here, we did not consider the impact of the movement



of this material, as the Stokes equations ignore the inertia of the model. It poses, however, the following question: does the movement of surrounding materials impact the horizontal pressure applied by them on the boundaries of the model? In which case, the traction would have to be changed accordingly.

The tests done on the boundary conditions of the analogue experiment model also showed that the material properties used at this point did not allow the restoration of the model. To study their impact and to find the ‘best’ effective properties inside the model, a design of experiment was used, and the restoration scheme was applied to eight models with different properties. As the viscosity of the silicone and the density of all materials were known, the parameters we studied were the viscosity inside the faults and the viscosity in the sand and pyrex layers. The first experiments helped narrow down the range of values for these effective viscosities, and showed that a different effective viscosity has to be used for each fault in the model. Various experiments then allowed us to tune the viscosity inside the faults accordingly, and decrease the restoration error. This viscosity tuning, however, was done manually and we could not find a relation between the viscosity difference between the faults, and their difference in age or shear band thickness. More tests using a local criterion on the fault throw for each fault may then be necessary to find how to guide the choice of the fault effective viscosity.

In order to add yet more physics, other simplifications could be lifted, which would require further tests to assess the impact of their removal. For example, we considered the viscosity as independent from time and from the layering of the model. It could be interesting, however, to study the influence of accumulated strain (by considering the sand and pyrex layers as visco-elastic materials) or of a variable viscosity in the layers (depending on the type of layer, or on the age and altitude, for example).

An issue that remains to be addressed is the fact that a lower viscosity inside the faults can lead to over-estimations of the horizontal velocity for the faults. In restoration simulations, this leads to the material inside some of the faults being pushed out by the blocks with higher viscosities on the sides. The application of an anisotropic viscosity may remove this issue, but has not been studied yet.

To further assess the creeping flow method potential, it would also be interesting to apply it to other structural models. The use of other analogue experiment setups, first, would allow to check the validity of the conditions that were found on this one. It would also provide the effective properties in a wider range of model deformation types. The comparison of the effective viscosity in different analogue models, for example, could provide interesting data when scaling the effective properties to apply the method on models of the subsurface at geological time scales.

While adding more physical conditions to geomechanical restoration is interesting in itself, the goal is also to provide a working method for the restoration of models describing the subsurface in real cases. Several questions would then arise. First, the boundary conditions may be more complicated, with the addition of continuous erosion and sedimentation on the topography (compared to punctual sedimentation in the analogue experiment). The forces at play several kilometers deep in the underground are also unknown, and the bottom boundary may be more complex than the free-slip and no-slip conditions applied here. For example, specific flow due to uplift or subsidence of the layers below the model may need to be taken into account. The pressure applied on the lateral boundaries may also prove to be more challenging than a Neumann traction based on the horizontal report of the lithostatic pressure (in which, by the way, uncertainty on the Poisson coefficient value



can be large). Indeed, other sources may have an impact on the applied pressure, such as a higher altitude or denser material near the boundary. Finally, the space of material parameters to be estimated would be much bigger than that of an analogue experiment model. It would then be useful to find a way to scale the effective parameters from those that were found in analogue experiments with deformation mechanisms analogue to the real-case models. Interestingly, to answer these questions, creeping
440 flow restoration could be a useful tool, because the conditions that best balance the models could be determined as the solution of an inverse problem on the restoration results, using the flattening condition as a likelihood metric.

7 Conclusions

In this paper, we have shown the results obtained with the creeping flow restoration method on a complex structural model including various faults. The first results start with fully kinematic boundary conditions, showing that conclusive results can
445 be obtained while changing the consideration of salt layers and faults to a more physical behavior, compared to previous geomechanical restoration schemes using elastic behavior. In order to go further, other boundary conditions were introduced. While the deformation is then *a priori* more physical, these conditions leave more freedom to the model velocity, and as such are more sensitive to the material parameters.

Using these boundary conditions, however, it was possible to assess the impact of changing the material properties inside the
450 model. By going closer to the effective material properties, we were then able to obtain results better than those using kinematic boundary conditions for the restoration. These results, however, both improved the physical meaning of the restoration, and provided valuable information on the effective material properties to use in mechanical simulations.

As such, the creeping flow restoration of this analogue experiment model showed that this restoration scheme can be applied
455 to complex real-case structural models, as well as some of the additional data that can be obtained from it. It also opened the way to a number of possible tests that could be performed to find out more on the effective material properties inside structural models, particularly when applying the method to geological models.

Author contributions. The writing of this paper, as well as the code of the software and the results, was done by M S-S. GC and PC provided useful discussions on the subject, guidance on solving the different problems, and funding for the PhD thesis that allowed this research through the RING-Gocad consortium. All authors contributed to the conceptualization, the design of experiments and the analysis of results.
460 GC and PC also helped with useful feedback and corrections on the manuscript.

Competing interests. The authors declare that they have no conflict of interests.

<https://doi.org/10.5194/egusphere-2023-2039>
Preprint. Discussion started: 28 September 2023
© Author(s) 2023. CC BY 4.0 License.



Acknowledgements. This project was done in the frame of the RING project, in the GeoRessources laboratory. We would like to thank for their support the academic and industrial sponsors of the RING-GOCAD Consortium managed by ASGA (<https://www.ring-team.org/consortium>). We would also like to thank Cedric Thieulot for valuable discussions and suggestions on this work.



465 References

- Al-Fahmi, M. M., Plesch, A., Shaw, J. H., and Cole, J. C.: Restorations of faulted domes, *AAPG Bulletin*, 100, 151–163, <https://doi.org/10.1306/08171514211>, 2016.
- Allen, P. A. and Allen, J. R.: *Basin analysis: Principles and application to petroleum play assessment*, John Wiley & Sons, 2013.
- Arndt, D., Bangerth, W., Clevenger, T. C., Davydov, D., Fehling, M., Garcia-Sanchez, D., Harper, G., Heister, T., Heltai, L., Kronbichler, M., Kynch, R. M., Maier, M., Pelteret, J.-P., Turcksin, B., and Wells, D.: The deal.II Library, Version 9.1, *Journal of Numerical Mathematics*, <https://doi.org/10.1515/jnma-2019-0064>, accepted, 2019.
- 470 Arndt, D., Bangerth, W., Davydov, D., Heister, T., Heltai, L., Kronbichler, M., Maier, M., Pelteret, J.-P., Turcksin, B., and Wells, D.: The deal. II finite element library: Design, features, and insights, *Computers & Mathematics with Applications*, <https://doi.org/10.1016/j.camwa.2020.02.022>, 2020.
- 475 Asgari, A. and Moresi, L.: Multiscale Particle-In-Cell Method: From Fluid to Solid Mechanics, in: *Advanced Methods for Practical Applications in Fluid Mechanics*, edited by Jones, S. A., chap. 9, IntechOpen, Rijeka, <https://doi.org/10.5772/26419>, 2012.
- Athy, L. F.: Density, porosity, and compaction of sedimentary rocks, *AAPG Bulletin*, 14, 1–24, <https://doi.org/10.1306/3D93289E-16B1-11D7-8645000102C1865D>, 1930.
- Bangerth, W., Hartmann, R., and Kanschat, G.: deal.II – a General Purpose Object Oriented Finite Element Library, *ACM Trans. Math. Softw.*, 33, 24/1–24/27, <https://doi.org/10.1145/1268776.1268779>, 2007.
- 480 Bouziat, A., Guy, N., Frey, J., Colombo, D., Colin, P., Cacas-Stentz, M.-C., and Cornu, T.: An Assessment of Stress States in Passive Margin Sediments: Iterative Hydro-Mechanical Simulations on Basin Models and Implications for Rock Failure Predictions, *Geosciences*, 9, 469, <https://doi.org/10.3390/geosciences9110469>, 2019.
- Buiter, S. J., Schreurs, G., Albertz, M., Gerya, T. V., Kaus, B., Landry, W., le Pourhiet, L., Mishin, Y., Egholm, D. L., Cooke, M., Maillot, B., Thieulot, C., Crook, T., May, D., Souloumiac, P., and Beaumont, C.: Benchmarking numerical models of brittle thrust wedges, *Journal of Structural Geology*, 92, 140–177, <https://doi.org/10.1016/j.jsg.2016.03.003>, 2016.
- 485 Chamberlin, R. T.: The Appalachian folds of central Pennsylvania, *The Journal of Geology*, 18, 228–251, <https://doi.org/10.1086/621722>, 1910.
- Chauvin, B.: *Applicability of the mechanics-based restoration: boundary conditions, fault network and comparison with a geometrical method*, Ph.D. thesis, Université de Lorraine, 2017.
- 490 Chauvin, B. P., Lovely, P. J., Stockmeyer, J. M., Plesch, A., Caumon, G., and Shaw, J. H.: Validating novel boundary conditions for three-dimensional mechanics-based restoration: An extensional sandbox model example, *AAPG Bulletin*, 102, 245–266, <https://doi.org/10.1306/0504171620817154>, 2018.
- Cobbold, P., Rossello, E., and Vendeville, B.: Some experiments on interacting sedimentation and deformation above salt horizons, *Bulletin de la Société Géologique de France*, pp. 453–460, 1989.
- 495 Cobbold, P. R. and Percevault, M.-N.: Spatial integration of strains using finite elements, in: *Strain Patterns in Rocks*, edited by Cobbold, P., Schwerdtner, W., and Treagus, S., pp. 299–305, Pergamon, <https://doi.org/10.1016/B978-0-08-030273-7.50010-0>, 1983.
- Courant, R., Friedrichs, K., and Lewy, H.: Über die partiellen Differenzgleichungen der mathematischen Physik, *Mathematische annalen*, 100, 32–74, <https://doi.org/10.1007/BF01448839>, 1928.
- 500 Dahlstrom, C.: Balanced cross sections, *Canadian Journal of Earth Sciences*, 6, 743–757, <https://doi.org/10.1139/e69-069>, 1969.



- De Santi, M. R., Campos, J. L. E., and Martha, L. F.: A Finite Element approach for geological section reconstruction, in: Proceedings of the 22th Gocad Meeting, Nancy, France, pp. 1–13, Citeseer, 2002.
- Dimakis, P., Braathen, B. I., Faleide, J. I., Elverhøi, A., and Gudlaugsson, S. T.: Cenozoic erosion and the preglacial uplift of the Svalbard–Barents Sea region, *Tectonophysics*, 300, 311–327, [https://doi.org/10.1016/S0040-1951\(98\)00245-5](https://doi.org/10.1016/S0040-1951(98)00245-5), 1998.
- 505 Donea, J., Huerta, A., Ponthot, J.-P., and Rodriguez-Ferran, A.: Arbitrary Lagrangian-Eulerian Methods, volume 1 of *Encyclopedia of Computational Mechanics*, chapter 14, John Wiley & Sons Ltd, 3, 1–25, <https://doi.org/10.1002/9781119176817.ecm2009>, 2004.
- Durand-Riard, P., Caumon, G., and Muron, P.: Balanced restoration of geological volumes with relaxed meshing constraints, *Computers & Geosciences*, 36, 441–452, <https://doi.org/10.1016/j.cageo.2009.07.007>, 2010.
- Durand-Riard, P., Salles, L., Ford, M., Caumon, G., and Pellerin, J.: Understanding the evolution of syn-depositional folds: Coupling decom-
510 paction and 3D sequential restoration, *Marine and Petroleum Geology*, 28, 1530–1539, <https://doi.org/10.1016/j.marpetgeo.2011.04.001>, 2011.
- Durand-Riard, P., Guzowski, C., Caumon, G., and Titeux, M.-O.: Handling natural complexity in three-dimensional geomechanical restoration, with application to the recent evolution of the outer fold and thrust belt, deep-water Niger Delta, *AAPG bulletin*, 97, 87–102, <https://doi.org/10.1306/06121211136>, 2013a.
- 515 Durand-Riard, P., Shaw, J. H., Plesch, A., and Lufadeju, G.: Enabling 3D geomechanical restoration of strike-and oblique-slip faults using geological constraints, with applications to the deep-water Niger Delta, *Journal of Structural Geology*, 48, 33–44, <https://doi.org/10.1016/j.jsg.2012.12.009>, 2013b.
- Fernandez, N.: 2D and 3D numerical modelling of multilayer detachment folding and salt tectonics, Ph.D. thesis, Mainz University, <https://doi.org/10.25358/openscience-2916>, 2014.
- 520 Fletcher, R. C. and Pollard, D. D.: Can we understand structural and tectonic processes and their products without appeal to a complete mechanics?, *Journal of Structural Geology*, 21, 1071–1088, [https://doi.org/10.1016/S0191-8141\(99\)00056-5](https://doi.org/10.1016/S0191-8141(99)00056-5), 1999.
- Fossen, H.: *Structural geology*, Cambridge University Press, second edn., 2016.
- Gassmüller, R., Lokavarapu, H., Heien, E., Puckett, E. G., and Bangerth, W.: Flexible and Scalable Particle-in-Cell Methods With Adaptive Mesh Refinement for Geodynamic Computations, *Geochemistry, Geophysics, Geosystems*, 19, 3596–3604,
525 <https://doi.org/10.1029/2018GC007508>, 2018.
- Gassmüller, R., Lokavarapu, H., Bangerth, W., and Puckett, E. G.: Evaluating the accuracy of hybrid finite element/particle-in-cell methods for modelling incompressible Stokes flow, *Geophysical Journal International*, 219, 1915–1938, <https://doi.org/10.1093/gji/ggz405>, 2019.
- Gratier, J.-P.: *L'équilibrage des coupes géologiques. Buts, méthodes et applications.*, Géosciences-Rennes, 1988.
- Groshong, R.: *3-D structural geology*, Springer, Berlin, Heidelberg, <https://doi.org/10.1007/978-3-540-31055-6>, 2006.
- 530 Guzowski, C. A., Mueller, J. P., Shaw, J. H., Muron, P., Medwedeff, D. A., Bilotti, F., and Rivero, C.: Insights into the mechanisms of fault-related folding provided by volumetric structural restorations using spatially varying mechanical constraints, *AAPG bulletin*, 93, 479–502, <https://doi.org/10.1306/11250807130>, 2009.
- Hall, J.: II. On the Vertical Position and Convolutions of certain Strata, and their relation with Granite, *Transactions of the Royal Society of Edinburgh*, 7, 79–108, <https://doi.org/10.1017/S0080456800019268>, 1815.
- 535 IFP and C&C Reservoirs: Principles of Digital Structural Analog Modeling, Tech. rep., 2006.
- Ismail-Zadeh, A. and Tackley, P.: *Computational methods for geodynamics*, Cambridge University Press, <https://doi.org/10.1017/CBO9780511780820>, 2010.



- Ismail-Zadeh, A., Tsepelev, I., Talbot, C., and Korotkii, A.: Three-dimensional forward and backward modelling of diapirism: numerical approach and its applicability to the evolution of salt structures in the Pricaspian basin, *Tectonophysics*, 387, 81–103, <https://doi.org/10.1016/j.tecto.2004.06.006>, 2004.
- Ismail-Zadeh, A. T., Talbot, C. J., and Volozh, Y. A.: Dynamic restoration of profiles across diapiric salt structures: numerical approach and its applications, *Tectonophysics*, 337, 23–38, [https://doi.org/10.1016/S0040-1951\(01\)00111-1](https://doi.org/10.1016/S0040-1951(01)00111-1), 2001.
- Kaus, B. J. and Podladchikov, Y. Y.: Forward and reverse modeling of the three-dimensional viscous Rayleigh-Taylor instability, *Geophysical Research Letters*, 28, 1095–1098, <https://doi.org/10.1029/2000GL011789>, 2001.
- Kaus, B. J., Mühlhaus, H., and May, D. A.: A stabilization algorithm for geodynamic numerical simulations with a free surface, *Physics of the Earth and Planetary Interiors*, 181, 12–20, <https://doi.org/10.1016/j.pepi.2010.04.007>, 2010.
- Kocher, T. and Mancktelow, N. S.: Dynamic reverse modelling of flanking structures: a source of quantitative kinematic information, *Journal of Structural Geology*, 27, 1346–1354, <https://doi.org/10.1016/j.jsg.2005.05.007>, 2005.
- Kronbichler, M., Heister, T., and Bangerth, W.: High accuracy mantle convection simulation through modern numerical methods, *Geophysical Journal International*, 191, 12–29, <https://doi.org/10.1111/j.1365-246X.2012.05609.x>, 2012.
- Lechmann, S. M., Schmalholz, S. M., Burg, J.-P., and Marques, F.: Dynamic unfolding of multilayers: 2D numerical approach and application to turbidites in SW Portugal, *Tectonophysics*, 494, 64–74, <https://doi.org/10.1016/j.tecto.2010.08.009>, 2010.
- Lovely, P., Flodin, E., Guzowski, C., Maerten, F., and Pollard, D. D.: Pitfalls among the promises of mechanics-based restoration: Addressing implications of unphysical boundary conditions, *Journal of Structural Geology*, 41, 47–63, <https://doi.org/10.1016/j.jsg.2012.02.020>, 2012.
- Lovely, P. J., Jayr, S. N., and Medwedeff, D. A.: Practical and efficient three-dimensional structural restoration using an adaptation of the GeoChron model, *AAPG Bulletin*, 102, 1985–2016, <https://doi.org/10.1306/03291817191>, 2018.
- Maerten, F. and Maerten, L.: Unfolding and Restoring Complex Geological Structures Using Linear Elasticity Theory, in: *AGU Fall Meeting Abstracts*, vol. 2001, pp. T22C–0940, 2001.
- Maerten, L. and Maerten, F.: Chronologic modeling of faulted and fractured reservoirs using geomechanically based restoration: Technique and industry applications, *AAPG bulletin*, 90, 1201–1226, <https://doi.org/10.1306/02240605116>, 2006.
- Massimi, P., Quarteroni, A., and Scrofani, G.: An adaptive finite element method for modeling salt diapirism, *Mathematical Models and Methods in Applied Sciences*, 16, 587–614, <https://doi.org/10.1142/S0218202506001273>, 2006.
- Massot, J.: Implémentation de méthodes de restauration équilibrée 3D, Ph.D. thesis, Institut National Polytechnique de Lorraine, 2002.
- Moretti, I.: Working in complex areas: New restoration workflow based on quality control, 2D and 3D restorations, *Marine and Petroleum Geology*, 25, 205–218, <https://doi.org/10.1016/j.marpetgeo.2007.07.001>, 2008.
- Moretti, I., Lepage, F., and Guiton, M.: KINE3D: a new 3D restoration method based on a mixed approach linking geometry and geomechanics, *Oil & Gas Science and Technology*, 61, 277–289, <https://doi.org/10.2516/ogst:2006021>, 2006.
- Muron, P.: Méthodes numériques 3-D de restauration des structures géologiques faillées, Ph.D. thesis, INPL, 2005.
- Parquer, M. N., Collon, P., and Caumon, G.: Reconstruction of Channelized Systems Through a Conditioned Reverse Migration Method, *Mathematical Geosciences*, 49, 965–994, <https://doi.org/10.1007/s11004-017-9700-3>, 2017.
- Ramberg, H.: Gravity, deformation and the earth's crust: in theory, experiments and geological application, London ; New York : Academic Press, 2d ed edn., 1981.
- Ramón, M. J., Pueyo, E. L., Caumon, G., and Briz, J. L.: Parametric unfolding of flexural folds using palaeomagnetic vectors, *Geological Society, London, Special Publications*, 425, 247–258, <https://doi.org/10.1144/SP425.6>, 2016.
- Rouby, D.: Restauration en carte des domaines faillés en extension. Méthode et applications., Ph.D. thesis, Université Rennes 1, 1994.



- Royden, L. and Keen, C.: Rifting process and thermal evolution of the continental margin of eastern Canada determined from subsidence curves, *Earth and Planetary Science Letters*, 51, 343–361, [https://doi.org/10.1016/0012-821X\(80\)90216-2](https://doi.org/10.1016/0012-821X(80)90216-2), 1980.
- Schmalholz, S. M.: 3D numerical modeling of forward folding and reverse unfolding of a viscous single-layer: Implications for the formation of folds and fold patterns, *Tectonophysics*, 446, 31–41, <https://doi.org/10.1016/j.tecto.2007.09.005>, 2008.
- 580 Schreurs, G., Buitter, S. J., Boutelier, J., Burberry, C., Callot, J.-P., CavoZZi, C., Cerca, M., Chen, J.-H., Cristallini, E., Cruden, A. R., Cruz, L., Daniel, J.-M., Da Poian, G., Garcia, V. H., Gomes, C. J., Grall, C., Guillot, Y., Guzmán, C., Hidayah, T. N., Hilley, G., Klinkmüller, M., Koyi, H. A., Lu, C.-Y., Maillot, B., Meriaux, C., Nilfouroushan, F., Pan, C.-C., Pillot, D., Portillo, R., Rose-
nau, M., Schellart, W. P., Schlische, R. W., Take, A., Vendeville, B., Vergnaud, M., Vettori, M., Wang, S.-H., Withjack, M. O.,
Yagupsky, D., and Yamada, Y.: Benchmarking analogue models of brittle thrust wedges, *Journal of Structural Geology*, 92, 116–139,
585 <https://doi.org/https://doi.org/10.1016/j.jsg.2016.03.005>, 2016.
- Schuh-Senlis, M., Thieulot, C., Cupillard, P., and Caumon, G.: Towards the application of Stokes flow equations to structural restoration simulations, *Solid Earth*, 11, 1909–1930, <https://doi.org/10.5194/se-11-1909-2020>, 2020.
- Stockmeyer, J. M. and Guzofski, C.: Interplay between extension, salt and pre-existing structure, offshore Angola, in: *AAPG Annual Convention and Exhibition*, 2014.
- 590 Tang, P., Wang, C., and Dai, X.: A majorized Newton-CG augmented Lagrangian-based finite element method for 3D restoration of geological models, *Computers & Geosciences*, 89, 200–206, <https://doi.org/10.1016/j.cageo.2016.01.013>, 2016.
- Thielmann, M., May, D., and Kaus, B.: Discretization errors in the hybrid finite element particle-in-cell method, *Pure and Applied Geophysics*, 171, 2165–2184, <https://doi.org/10.1007/s00024-014-0808-9>, 2014.
- Trim, S., Lowman, J., and Butler, S.: Improving mass conservation with the tracer ratio method: application to thermochemical mantle flows,
595 *Geochemistry, Geophysics, Geosystems*, 21, e2019GC008 799, <https://doi.org/10.1029/2019GC008799>, 2020.
- Willis, B.: *The mechanics of Appalachian structure*, vol. 13, US Government Printing Office, 1894.